Journal of Sound and Vibration 326 (2009) 251–262

Contents lists available at ScienceDirect

Journal of Sound and Vibration

journal homepage: www.elsevier.com/locate/jsvi

Vibration analysis and measurement for piezoceramic rectangular plates in resonance

Chen-Pang Chen *, Chi-Hung Huang, Yi-Yu Chen

Department of Mechanical Engineering, Ching Yun University, Chung-Li, Taiwan 320, China

ARTICLE INFO

Article history:
Received 6 August 2008
Received in revised form
15 April 2009
Accepted 18 April 2009
Handling Editor: L.G. Tham
Available online 17 May 2009

ABSTRACT

In this paper the transverse vibration characteristics of piezoceramic rectangular plates, with completely free and completely clamped boundary conditions, are investigated by theoretical analysis, experimental measurement, and numerical calculation. Using Ritz's method together with the equivalent material constants carries out the theoretical evaluations for resonant frequencies. Two optical techniques, amplitude-fluctuation electronic speckle pattern interferometry (AF-ESPI) and laser Doppler vibrometer (LDV), based on the displacement measurement are employed to determine the transverse vibration modes. In addition, the impedance analyzer is also used to measure the electrical impedance variation. From the experimental results, it is found that the transverse vibration modes cannot be obtained by impedance analysis for the completely free piezoceramic plate; however, certain modes can be unexpectedly measured for the completely clamped piezoceramic plate owing to the imperfect boundary simulation in experiments. Numerical calculations using the finite element method (FEM) are performed and good agreement is obtained when comparing the theoretical analysis and experimental measurements. According to the theoretical analysis, frequency parameter versus equivalent Poisson's ratios ranging from 0.25 to 0.6 with different aspect ratios and material types are also presented for the first three transverse modes.

1. Introduction

It is well known that piezoelectric materials have been widely used in electromechanical sensors and actuators, ultrasonic devices, electro-optic modulators, etc. In studying the vibration characteristics of piezoelectric materials, researchers paid more attention to the crystals in the early periods of research. Dökmecí [1] reviewed the representative applications to vibrations for one- and two-dimensional crystals with some different configurations before 1980. Due to the difficulty of manufacture and the limitations of crystallographic directions for crystals, piezoelectric ceramics made of lead zirconate titanate (PZT) have been adopted for most engineering applications in the past few decades. These piezoceramics have the advantages of lower cost, higher mechanical strength, better piezoelectric activity, and easier shape forming. Although the vibration characteristics of piezoelectric plates can be analytically determined by linear piezoelectricity and plate theory [2]; completely exact solutions are obtained usually for circular or annular types with certain simplifications. Ivina [3] studied the symmetric modes of vibration for circular piezoelectric plates to determine the resonant and anti-resonant frequencies, radial mode configurations, and the optimum geometrical dimensions to maximize the dynamic

* Corresponding author. Tel.: +886 3 4581196; fax: +886 3 4683301.
E-mail address: cpchen@cyu.edu.tw (C.-P. Chen).

0022-460X/$ - see front matter © 2009 Elsevier Ltd. All rights reserved.
doi:10.1016/j.jsv.2009.04.025

electromechanical coupling coefficient. Huang et al. [4] investigated the vibration of thin piezoceramic disks with completely free boundary conditions for transverse, tangential and radial extensional modes by theoretical analysis, numerical simulation, and experimental measurement. Huang [5] discussed the transverse vibration of piezoceramic annular plates with four different boundary conditions (free–free, fixed–fixed, free–fixed, and fixed–free) and then classified the variation of resonant frequencies into three groups.

In general, the theoretical analysis for piezoelectric rectangular plates is more complicated because there is no exact solution to the governing equations. Regarding the manipulation for elastic rectangular plates, the series-form trigonometric or trial functions are usually employed to satisfy the electrical or mechanical boundary conditions. Holland [6] used the Rayleigh–Ritz method to study the extensional modes of PZT rectangular plates and classified the modes into four distinct symmetry types. Lee and Jiang [7] derived the state space method to obtain solutions for a piezoelectric rectangular plate with simply supported boundary conditions. Eight state variables (three displacement components, electrical potential, three out-of-plane stresses, and transverse electrical displacement) were investigated and the results were compared with the purely elastic case. Moreover, Chen et al. [8] presented the non-dimensional state equations to simplify the free vibration analysis of simply-supported piezoelectric ceramic plates. Batra and Liang [9] considered the effect and optimization of simply-supported rectangular laminated plates with embedded PZT layers as vibrating close to resonance. Chang and Tung [10] developed the electro-elastic theory with the Kirchhoff–Love hypothesis to obtain the electromechanical characteristics of two-layered rectangular laminated plates with completely clamped edges. By experimental measurement and FEM calculations, Ma and Lin [11] investigated the transverse vibration of piezoceramic rectangular plates with completely free and completely fixed boundary conditions. Ramirez et al. [12,13] developed a discrete-layer model to investigate the free vibration behavior of magneto-electro-elastic laminates and graded composite plates. Rectangular composite plates with different boundary conditions, aspect ratios, and gradation types were studied in their work.

Referring to the literature, the transverse vibration characteristics were usually investigated for the piezoceramic laminated plates or bimorphs; moreover, most of articles presented the theoretical or numerical analysis and only few experimental investigations were provided, especially by using the identification of resonant frequencies and the corresponding mode shapes. In this paper, the transverse vibration of piezoceramic rectangular plates with completely free (free–free–free–free, FFFF) and completely clamped (clamped–clamped–clamped–clamped, CCCC) edges are investigated in three aspects: theoretical analysis, numerical simulation, and experimental measurement. The theoretical calculation is carried out by Ritz's method together with the named equivalent constant method, as proposed by Huang [14]. By using the proposed methodology, the electrical field consideration is suppressed and the transverse vibration analysis of piezoceramic rectangular plates is undertaken once the corresponding conditions of isotropic plates are determined. To validate the theoretical results, this study utilizes two optical techniques, amplitude-fluctuation electronic speckle pattern interferometry (AF-ESPI) and laser Doppler vibrometer (LDV), and the impedance analyzer to experimentally investigate the vibration behavior of piezoceramic rectangular plates in resonance. The advantage of using the AF-ESPI method is that both resonant frequencies and the corresponding mode shapes can be obtained simultaneously from the experimental procedure. Besides the AF-ESPI measurement, the resonant frequencies measured by LDV system and impedance analyzer can provide additional information about the piezoceramic plate vibration. Commercially available finite element analysis software is also used to provide the numerical simulation of resonant frequencies and mode shapes. Good agreements of the resonant frequencies are obtained for theoretical, experimental, and numerical results; in addition, the mode shapes obtained by the AF-ESPI method also agree well with the numerical results. Based on the theoretical calculations, the dependence of transverse resonant frequencies on equivalent Poisson's ratio ranging from 0.25 to 0.6 is investigated with five different aspect ratios ($\frac{1}{3}, \frac{1}{2}, 1, 2$, and 3). To verify the suitability of the proposed theoretical analysis, one isotropic aluminum material (6061T6) and four piezoceramic materials ($BaTiO_3$, PZT-4, PZT-5, and PIC-151) are selected to perform the FEM calculations and then compare with the theoretical predictions.

2. Ritz's method with equivalent constants

For a piezoceramic thin plate vibrating at angular frequency ω, after suppressing the time-dependent term, the maximum potential and kinetic energy of the plate are given by

$$V_{\max} = \frac{\bar{D}}{2}\int\int\left[\left(\frac{\partial^2 W}{\partial x^2}\right)^2 + \left(\frac{\partial^2 W}{\partial y^2}\right)^2 + 2\bar{\nu}\frac{\partial^2 W}{\partial x^2}\frac{\partial^2 W}{\partial y^2} + 2(1-\bar{\nu})\left(\frac{\partial^2 W}{\partial x \partial y}\right)^2\right] \mathrm{d}x\,\mathrm{d}y \tag{1}$$

$$T_{\max} = \frac{1}{2}\rho h\omega^2 \int\int W^2\,\mathrm{d}x\,\mathrm{d}y \tag{2}$$

where $W = W(x,y)$ is the transverse deflection function, ρ is the density, and h is the plate thickness. In Eq. (1), the equivalent Poisson's ratio $\bar{\nu}$ and flexural rigidity $\bar{D}$ are defined as [14]

$$\bar{\nu} = \frac{2-(1-\nu_p)(2-k_p^2)}{2-(1-\nu_p)k_p^2} \tag{3}$$

$$\bar{D} = \frac{h^3}{12}\frac{2-(1-\nu_p)k_p^2}{2s_{11}^E(1-\nu_p^2)(1-k_p^2)} \tag{4}$$

where $\nu_p = -s_{12}^E/s_{11}^E$ is the planar Poisson's ratio, $k_p = \sqrt{2d_{31}^2/\varepsilon_{33}^T s_{11}^E(1-\nu_p)}$ is the planar electromechanical coupling coefficient, s_{11}^E and s_{12}^E are the compliance constants at constant electrical field, d_{31} is the piezoelectric constant, and ε_{33}^T is the dielectric constant at constant stress. By equating Eqs. (1) and (2), the resonant frequency f_r can be determined when $W(x,y)$ satisfies the mechanical boundary conditions and minimizes the expression as

$$\omega^2 = (2\pi f_r)^2 = \frac{2}{\rho h}\frac{V_{\max}}{\int\int W^2\,\mathrm{d}x\,\mathrm{d}y} \tag{5}$$

If the rectangular plate is bounded by the edges $x=0$, $x=a$, $y=0$, and $y=b$ as shown in Fig. 1, $W(x,y)$ can be represented as a linear series of assumed functions in the form of

$$W(x,y) = \sum_{m=1}^{p}\sum_{n=1}^{q} A_{mn}X_m(x)Y_n(y) \tag{6}$$

The beam functions $X_m(x)$ and $Y_n(y)$ are admissible so that the boundary conditions of the beams match those of the plate in the x- and y-direction, respectively; this will guarantee satisfaction of the essential boundary conditions. Three types of beam functions (clamped–clamped, clamped–free, and free–free) can be adopted to construct six cases for rectangular plates, including combinations of clamped or free boundary conditions. By substituting the expression of $W(x,y)$ into Eq. (5), the angular frequencies ω are minimized by taking the partial derivative with respect to each coefficient A_{mn}; this results in a system of linear homogeneous equations as follows:

$$\sum_{m=1}^{p}\sum_{n=1}^{q}[C_{mn}^{ij} - \lambda\delta_{mn}]A_{mn} = 0 \tag{7}$$

where

$$\lambda = \frac{\omega^2\rho h a^3 b}{\bar{D}} \tag{8}$$

$$\delta_{mn} = \begin{cases} 1 & \text{for } mn = ij \\ 0 & \text{for } mn \neq ij \end{cases}$$

and

$$C_{mn}^{ij} = \bar{\nu}\frac{a}{b}\left[\left(a\int_0^a X_m\frac{\mathrm{d}^2X_i}{\mathrm{d}x^2}\,\mathrm{d}x\right)\left(b\int_0^b Y_j\frac{\mathrm{d}^2Y_n}{\mathrm{d}y^2}\,\mathrm{d}y\right) + \left(a\int_0^a X_i\frac{\mathrm{d}^2X_m}{\mathrm{d}x^2}\,\mathrm{d}x\right)\left(b\int_0^b Y_n\frac{\mathrm{d}^2Y_j}{\mathrm{d}y^2}\,\mathrm{d}y\right)\right] + 2(1-\bar{\nu})\frac{a}{b}\left(a\int_0^a\frac{\mathrm{d}X_i}{\mathrm{d}x}\frac{\mathrm{d}X_m}{\mathrm{d}x}\,\mathrm{d}x\right)\left(b\int_0^b\frac{\mathrm{d}Y_j}{\mathrm{d}y}\frac{\mathrm{d}X_n}{\mathrm{d}y}\,\mathrm{d}y\right) \quad \text{for } mn\neq ij \tag{9-1}$$

$$C_{mn}^{ij} = \frac{a}{b}\varepsilon_m^4 + \left(\frac{a}{b}\right)^3\varepsilon_n^4 + 2\bar{\nu}\frac{a}{b}\left(a\int_0^a X_m\frac{\mathrm{d}^2X_m}{\mathrm{d}x^2}\,\mathrm{d}x\right)\left(b\int_0^b Y_n\frac{\mathrm{d}^2Y_n}{\mathrm{d}y^2}\,\mathrm{d}y\right) + 2(1-\bar{\nu})\frac{a}{b}\left(a\int_0^a\left(\frac{\mathrm{d}X_m}{\mathrm{d}x}\right)^2\mathrm{d}x\right)\left(b\int_0^b\left(\frac{\mathrm{d}Y_n}{\mathrm{d}y}\right)^2\mathrm{d}y\right) \quad \text{for } mn = ij \tag{9-2}$$

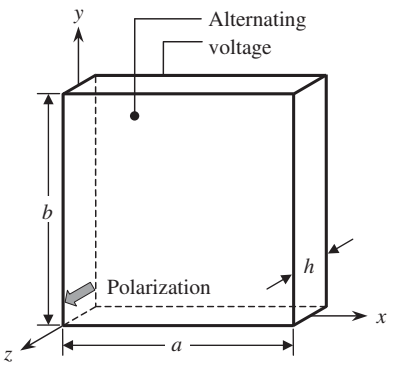

Fig. 1. Geometry and coordinate system of the piezoceramic rectangular plate.

In Eq. (9-2), the numerical values of ε_m and ε_n are given by Young [15]. The eigenvalues λ for resonant frequencies are obtained when the coefficient determinant of linear systems (Eq. (7)) equals zero. It is significant to note that, when the equivalent constants $\bar{v} = v$ and $\bar{D} = Eh^3/12(1-v^2)$, in which v is the Poisson's ratio and E is the Young's modulus, then the theoretical derivation will serve as the case for isotropic rectangular plates.

The theoretical calculations by Eq. (7) are carried out for a 36-term series by taking both m and n equal to 1, 2, 3, 4, 5, and 6. It is indicated that the corresponding 36 linear equations are divided into two groups, and then two corresponding 18×18 symmetric matrices are developed for the coefficient C_{mn}^{ij}. One of the two groups includes only $n = 1, 3, 5$ and represents the symmetrical modes with respect to the line $y = b/2$. The other group includes only $n = 2, 4, 6$ and stands for the anti-symmetrical modes with respect to the line $y = b/2$.

3. Principle of experimental technique

3.1. Amplitude-fluctuation electronic speckle pattern interferometry (AF-ESPI)

The most familiar way that ESPI is used for vibration analysis is the time-averaged method with an image sensor integrating the speckle interferogram field pixel by pixel. The term "time-averaged" implies that the vibration measurement includes many periods of object motion during the camera-capturing period. For the out-of-plane full-field vibration measurement using the AF-ESPI method, the first image is recorded as a reference after the specimen vibrates periodically. As the vibration of the specimen continues, the vibration amplitude changes from a to $a+\Delta a$ because of the electronic noise or instability of the apparatus. When the vibration amplitude variation Δa is small, the first image is subtracted from the second by the image processing system and the resulting image intensity can be expressed as

$$I = \frac{\sqrt{I_O I_R}}{2}\left|(\cos\,\Phi)\left[\frac{2\pi\Delta a}{\Lambda}(1+\cos\,\Psi)\right]^2 J_0\left[\frac{2\pi a}{\Lambda}(1+\cos\,\Psi)\right]\right| \tag{10}$$

where I_O is the object light intensity, I_R is the reference light intensity, Φ is the phase difference between object and reference light, Λ is the wavelength of laser, and Ψ is the angle between object light and observation direction.

In view of Eq. (10), it can be seen that the fringe patterns for the out-of-plane vibration obtained by AF-ESPI method are dominated by a zero-order Bessel function J_0; in fact, the fringe patterns for in-plane vibration exhibit characteristics similar to those for out-of-plane vibration. The AF-ESPI method was first proposed by Wang et al. [16] for transverse vibration measurement. Ma and Huang [17] provided a detailed discussion of the AF-ESPI method to investigate both the out-of-plane and in-plane vibrations of piezoelectric rectangular parallelepipeds for a three-dimensional configuration.

3.2. Laser Doppler vibrometer (LDV)

An optical technique, the laser Doppler vibrometer (LDV), is developed from the principle of the Michelson interferometer and the Doppler effect. The LDV measures the moving velocity or displacement of an object by detecting the frequency shift of the laser. For the LDV system, a built-in dynamic signal analyzer (DSA) composed of the dynamic signal analyzer software and a plug-in waveform generator board can provide the specimen with the swept-sine excitation signal. With the help of the emitting excitation by DSA, the LDV system measures the dynamic responses of the specimen by setting the beginning and ending frequencies for sweeping. In the analysis software, the swept-sine excitation signal is taken as input and the response measured by the LDV is converted into the voltage signal and is taken as the output. After the fast Fourier transform processing of the input and output with the DSA software, the ratio of output/input ("gain") is obtained.

4. A experimental investigations and theoretical discussions

The piezoceramic rectangular plates as shown in Fig. 1 with effective size $a = b = 40\,\text{mm}$, and thickness $h = 0.5\,\text{mm}$ are selected to perform experimental and numerical investigations. The model number of piezoceramics is PIC-151 (Germany Physik Instrument Company), whose material properties are listed in Table 1. Two opposite surfaces of the plate ($z = \pm h/2$) are completely covered by CuNi electrodes and the plate is excited by an alternating voltage across the two electroded surfaces. The thickness of the CuNi electrodes, which is applied by the sputtering technique, is in the range of $1\,\mu\text{m}$. Comparing with the plate thickness, the influence of the electrodes can be neglected for the experimental measurement and theoretical analysis. There are two types of mechanical boundary conditions, FFFF and CCCC, to be discussed in this study; as mentioned above, the symbols FFFF and CCCC represent piezoceramic rectangular plates with completely free and completely clamped edges, respectively. To realize the completely clamped conditions in the experimental measurement, the piezoceramic plate is mounted on a fixture by adhesive along all edges.

The full-field, time-averaged AF-ESPI optical systems are first used to perform the transverse (out-of-plane) vibration measurements. The advantage of using the AF-ESPI method is that both resonant frequencies and the corresponding mode shapes can be obtained simultaneously from the experimental procedure. A He–Ne laser with wavelength $\Lambda = 632.8\,\text{nm}$ is used as the coherent light source. We use a charge-coupled device (CCD) camera and a frame grabber with an onboard

Table 1
Material properties of 6061T6, $BaTiO_3$, PZT-4, PZT-5, and PIC-151.

Quantity	6061T6	$BaTiO_3$	PZT-4	PZT-5	PIC-151
s_{11}^E ($10^{-12}\,m^2\,N^{-1}$)	–	9.15	12.3	16.4	16.83
s_{33}^E	–	9.46	15.5	18.8	19.0
s_{12}^E	–	−2.75	−4.05	−5.74	−5.656
s_{13}^E	–	−2.89	−5.31	−7.22	−7.107
s_{44}^E	–	22.73	39.0	47.5	50.96
s_{66}^E	–	23.81	32.7	44.3	44.97
d_{31} ($10^{-12}\,m\,V^{-1}$)	–	−78.4	−123	−172	−214
d_{33}	–	190.8	289	374	423
d_{15}	–	259.1	496	584	610
ε_{11}^T ($10^{-9}\,F\,m^{-1}$)	–	15.792	13.054	15.31	17.134
ε_{33}^T	–	19.073	11.505	15.045	18.665
ρ ($kg\,m^{-3}$)	2700	5700	7500	7750	7800
v	0.33	–	–	–	–
E ($10^9\,N\,m^{-2}$)	70	–	–	–	–

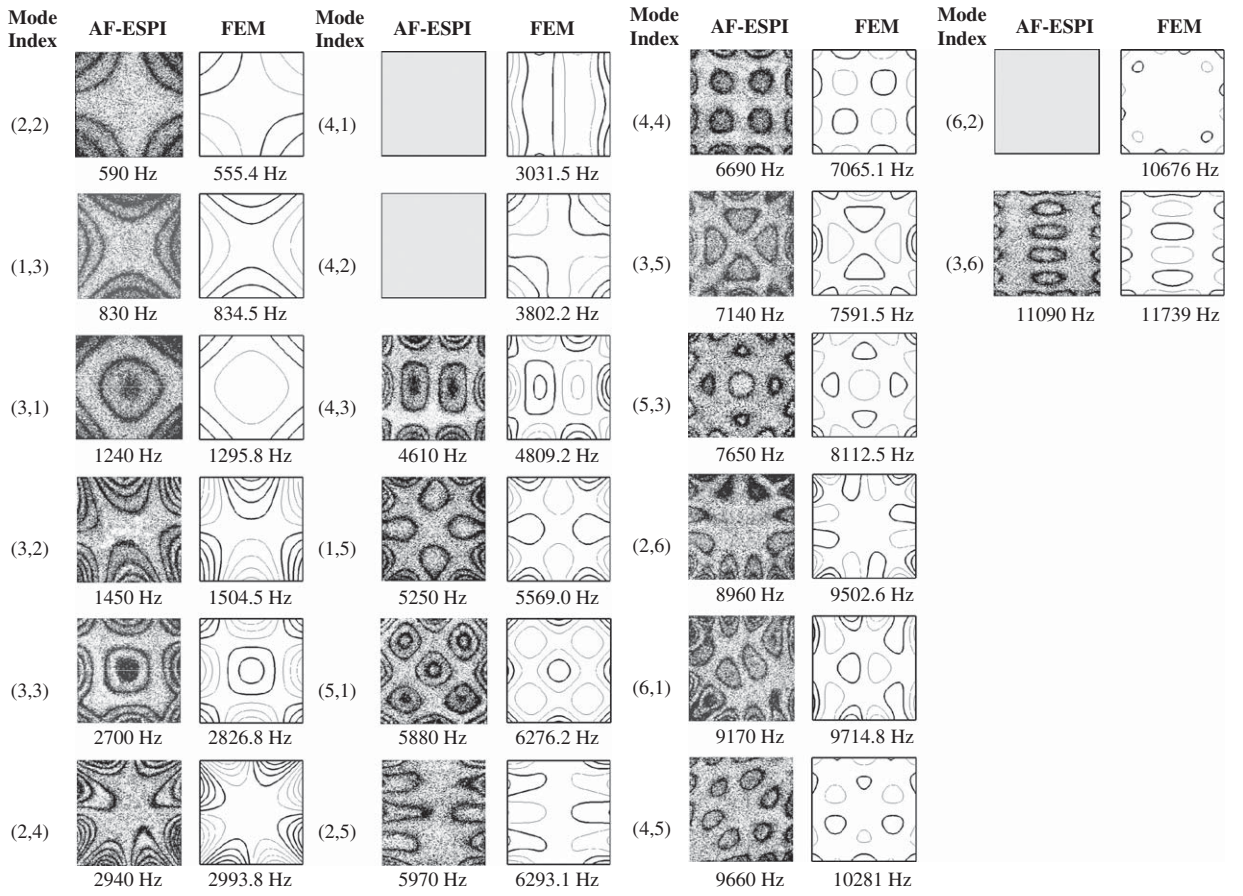

Fig. 2. The transverse vibration modes obtained by AF-ESPI and FEM for the FFFF piezoceramic plate.

digital signal processor to record and process the images. The laser beam is divided into two parts, the object and reference beam, by a beamsplitter. The object beam travels to the specimen and is then reflected to the CCD camera. The reference beam goes directly to the CCD camera via a mirror and a reference plate. Note that the optical path length and the light intensities of these two beams are maintained equal in the experimental setup. The CCD camera converts the intensity distribution of the interference pattern into a corresponding video signal at 30 frames per second. The signal is

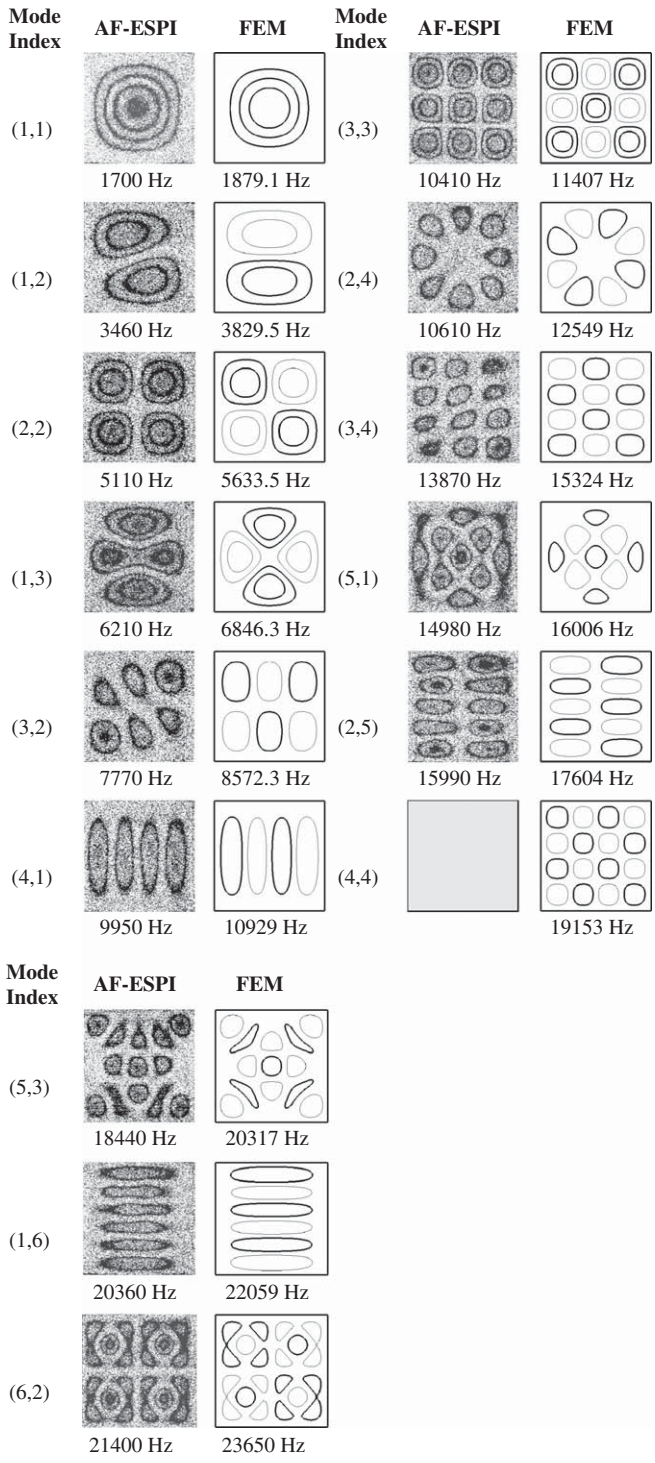

Fig. 3. The transverse vibration modes obtained by AF-ESPI and FEM for the CCCC piezoceramic plate.

electronically processed and finally converted into an image on the video monitor. The interpretation of the interference fringe image is similar to the reading of a contour map. As seen in the experimental results, the fringe pattern corresponds to the mode shape and the brightest fringes represent the nodal lines at resonance. Fig. 2 shows the experimental and numerical results for the first 20 mode shapes of the FFFF piezoceramic plate and Fig. 3 shows the first 15 mode shapes of the CCCC piezoceramic plate. In Figs. 2 and 3, we indicate the phase of displacement for finite element results as dark or

light lines, with the dark lines in the opposite direction to the light lines. The transition from dark lines to light lines corresponds to zero displacement lines, also called nodal lines. The zero-order fringe, which is the brightest fringe in the experimental results, represents the nodal lines of the vibrating piezoceramic plates at resonance. The mode index (m, n) shown in Figs. 2 and 3 indicates that the mode shape contains $(m-1)$ and $(n-1)$ nodal lines parallel to the y- and x-axis, respectively; however, this excludes the nodal lines along the clamped edges. The mode shapes obtained by AF-ESPI measurement can be checked by the nodal lines and fringe patterns with the numerical results. Excluding some mode

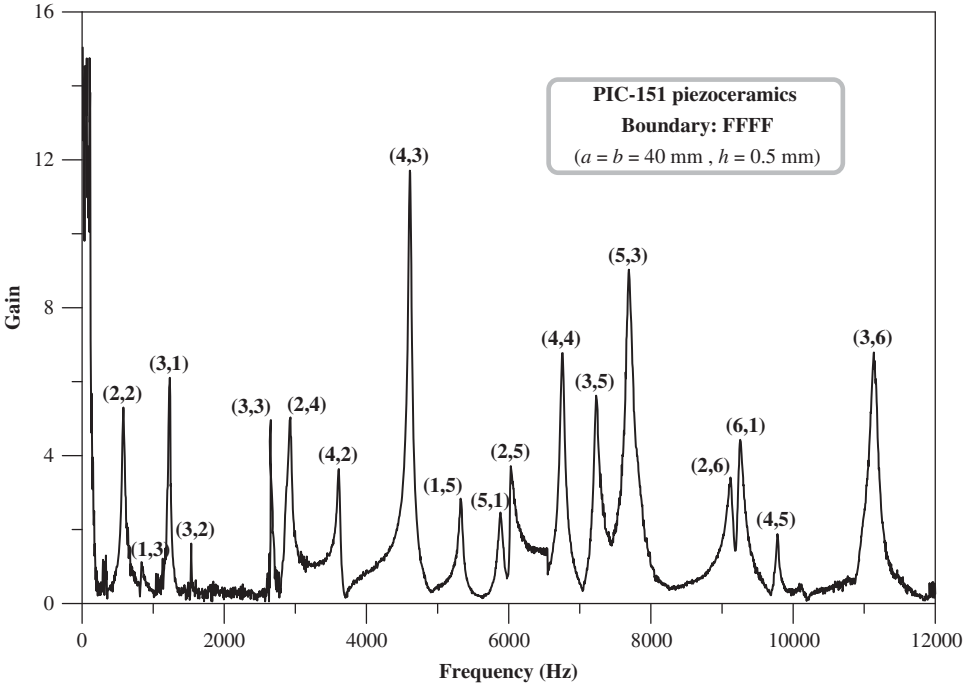

Fig. 4. LDV gain spectrum of transverse vibration modes for the piezoceramic FFFF plate.

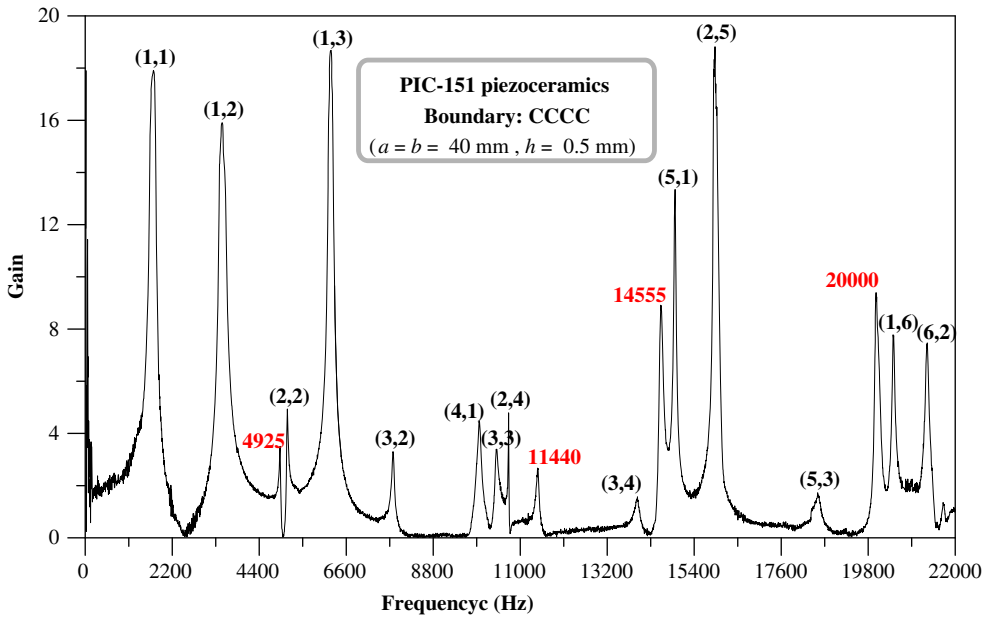

Fig. 5. LDV gain spectrum of transverse vibration modes for the piezoceramic CCCC plate.

Table 2
Results of transverse resonant frequencies obtained by theory, FEM, LDV, and AF-ESPI for the FFFF piezoceramic plate.

Mode index	(a) Theory (Hz)	(b) FEM (Hz)	(c) LDV (Hz)	(d) AF-ESPI (Hz)	Error (a)/(b) (%)	Difference (c)/(d) (%)
(2,2)	560.5	555.4	575	590	0.92	−2.54
(1,3)	879.0	834.5	835	830	5.33	0.60
(3,1)	1336.3	1295.8	1235	1240	3.13	−0.40
(3,2)	1566.2	1504.5	1535	1450	4.10	5.86
(3,3)	2913.0	2826.8	2655	2700	3.05	−1.67
(2,4)	3199.6	2993.8	2930	2940	6.87	−0.34
(4,1)	3160.5	3031.5	–	–	4.26	–
(4,2)	3994.5	3802.2	3610	–	5.06	–
(4,3)	4934.7	4809.2	4610	4610	2.61	0.00
(1,5)	5903.4	5569.0	5320	5250	6.00	1.33
(5,1)	6469.9	6276.2	5885	5880	3.09	0.09
(2,5)	6662.6	6293.1	6030	5970	5.87	1.01
(4,4)	7318.3	7065.1	6755	6690	3.58	0.97
(3,5)	7788.7	7591.5	7230	7140	2.60	1.26
(5,3)	8505.1	8112.5	7690	7650	4.84	0.52
(2,6)	10,652	9502.6	9120	8960	12.09	1.79
(6,1)	10,139	9714.8	9255	9170	4.36	0.93
(4,5)	10,663	10,281	9780	9660	3.72	1.24
(6,2)	11,282	10,676	–	–	5.68	–
(3,6)	12,286	11,739	11,135	11,090	4.66	0.41

Table 3
Results of transverse resonant frequencies obtained by theory, FEM, LDV, and AF-ESPI for the CCCC piezoceramic plate.

Mode index	(a) Theory (Hz)	(b) FEM (Hz)	(c) LDV (Hz)	(d) AF-ESPI (Hz)	Error (a)/(b) (%)	Difference (c)/(d) (%)
(1,1)	1868.9	1879.1	1725	1700	−0.54	1.47
(1,2)	3812.2	3829.5	3465	3460	−0.45	0.14
(2,2)	5624.9	5633.5	5115	5110	−0.15	0.10
(1,3)	6835.3	6846.3	6215	6210	−0.16	0.08
(3,2)	8580.0	8572.3	7780	7770	0.09	0.13
(4,1)	10,936	10,929	9970	9950	0.07	0.20
(3,3)	11,450	11,407	10,395	10,410	0.38	−0.14
(2,4)	12,600	12,549	10,705	10,610	0.41	0.90
(3,4)	15,434	15,324	13,970	13,870	0.72	0.72
(5,1)	16,061	16,006	14,920	14,980	0.34	−0.40
(2,5)	17,723	17,604	15,925	15,990	0.68	−0.41
(4,4)	19,380	19,153	–	–	1.18	–
(5,3)	20,528	20,317	18,525	18,440	1.04	0.46
(1,6)	22,740	22,059	20,440	20,360	3.09	0.39
(6,2)	25,821	23,650	21,300	21,400	9.18	−0.47

shapes that are too blurry to be captured by AF-ESPI, excellent agreement between experimental measurement and numerical simulation is found for both FFFF and CCCC piezoceramic plates.

To compare with the results obtained by AF-ESPI, the other point-wise optical technique called the laser Doppler vibrometer (LDV) (AVID, Ahead Optoelectronics Inc.) is also employed to measure the transverse vibration modes. The experimental gain spectrums of FFFF and CCCC piezoceramic plates are shown in Figs. 4 and 5, respectively; the peaks appearing in the frequency response curve stand for the resonant frequencies of transverse vibration. It is indicated that, for the CCCC piezoceramic plate shown in Fig. 5, there are four "additional" resonant frequencies being measured for which the corresponding mode indices could not be found. However, this unexpected situation does not occur with the FFFF piezoceramic plate, so this phenomenon should result from the imperfect simulation of clamped edges for the CCCC piezoceramic plate.

Table 2 shows the first 20 transverse resonant frequencies of the FFFF piezoceramic plate obtained by theoretical prediction, FEM calculation, LDV, and AF-ESPI; and Table 3 shows the results of first 15 transverse resonant frequencies for the CCCC piezoceramic plate. The FEM calculations of resonant frequencies as well as mode shapes are investigated by the ABAQUS finite element package [18]. The 20-node three-dimensional solid piezoelectric element "C3D20RE", standing for the 20-node quadratic brick element with reduced integration in ABAQUS, is selected for the numerical analysis. It is recognized that, in Tables 2 and 3, the theoretical predictions are generally higher than the finite element results, except for the first four modes of the CCCC piezoceramic plate. For the resonant frequencies of modes (2,4) and (4,1) in Table 2, the order of modes changes when comparing the results between theoretical and finite element calculations, and so do the

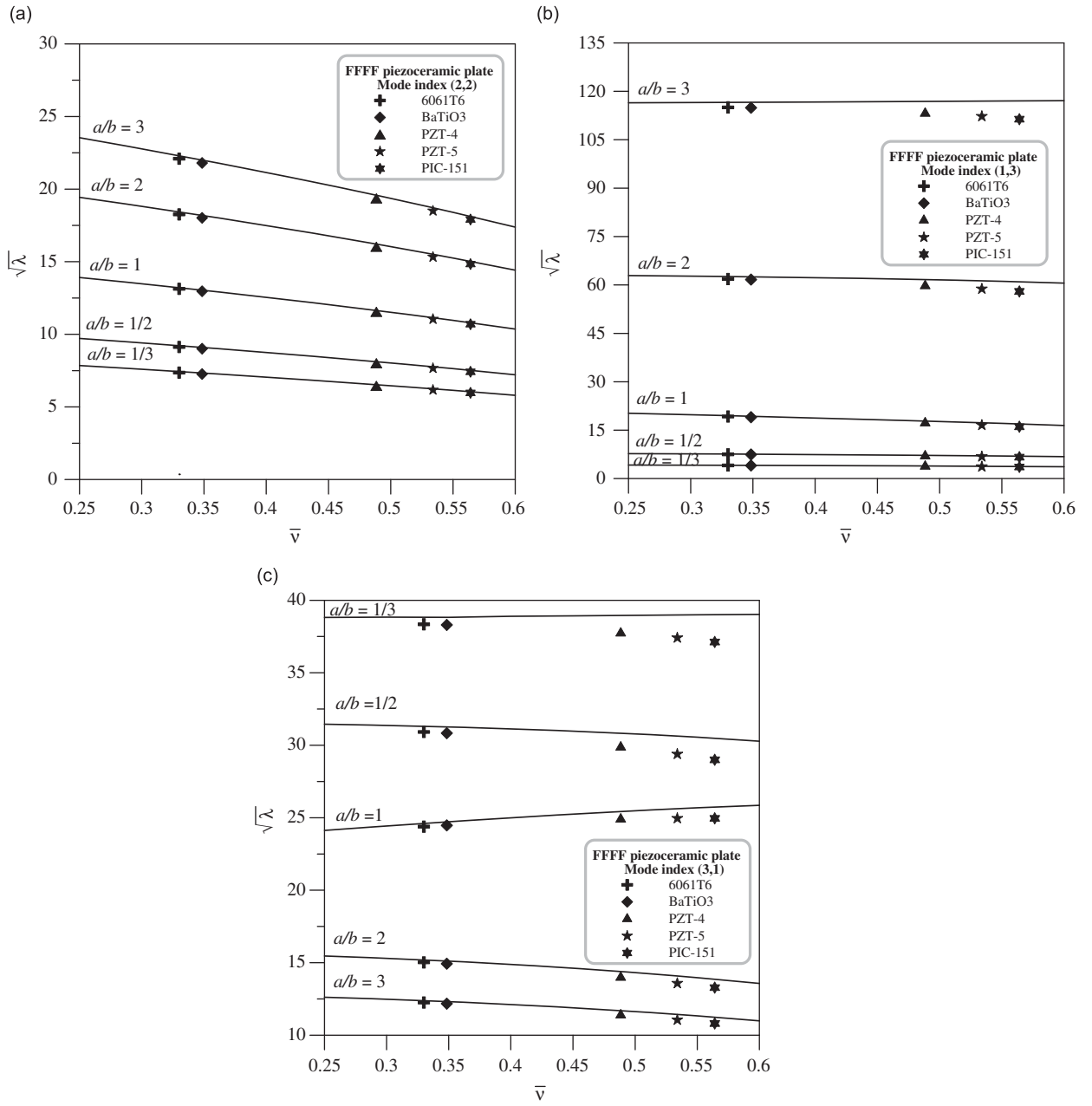

Fig. 6. Frequency parameter ($\sqrt{\lambda}$) versus equivalent Poisson's ratio ($\bar{\nu}$) for the mode indices: (a) (2,2), (b) (1,3), and (c) (3,1) with different aspect ratios (a/b).

modes (2,6) and (6,1). As shown in Tables 2 and 3, the theoretical predictions agree well with the finite element results, and the experimental results are also in good agreement between the AF-ESPI and LDV measurements. The error between theoretical and numerical results can be reduced by increasing the number of m and n, i.e., increasing the dimension of matrix C_{mn}^{ij}. The thickness of the piezoceramic plate also shows significant influence on the theoretical and numerical results. This is because the two-dimensional plate hypotheses and three-dimensional element simulations are employed for theoretical and FEM calculations, respectively. On the other hand, the discrepancies between theoretical and experimental values are probably due to the material constant accuracy, the numerical approximation method and, especially, the clamped boundary condition of the plate.

With reference to the different aspect ratios a/b, the dependence of transverse frequency parameter λ on equivalent Poisson's ratio $\bar{\nu}$ ranging from 0.25 to 0.6 is investigated. Figs. 6(a)–(c) show the results of the first three vibration modes versus different $\bar{\nu}$ for the FFFF piezoceramic plate, including mode indices (2,2), (1,3), and (3,1). In Fig. 6, the square root of

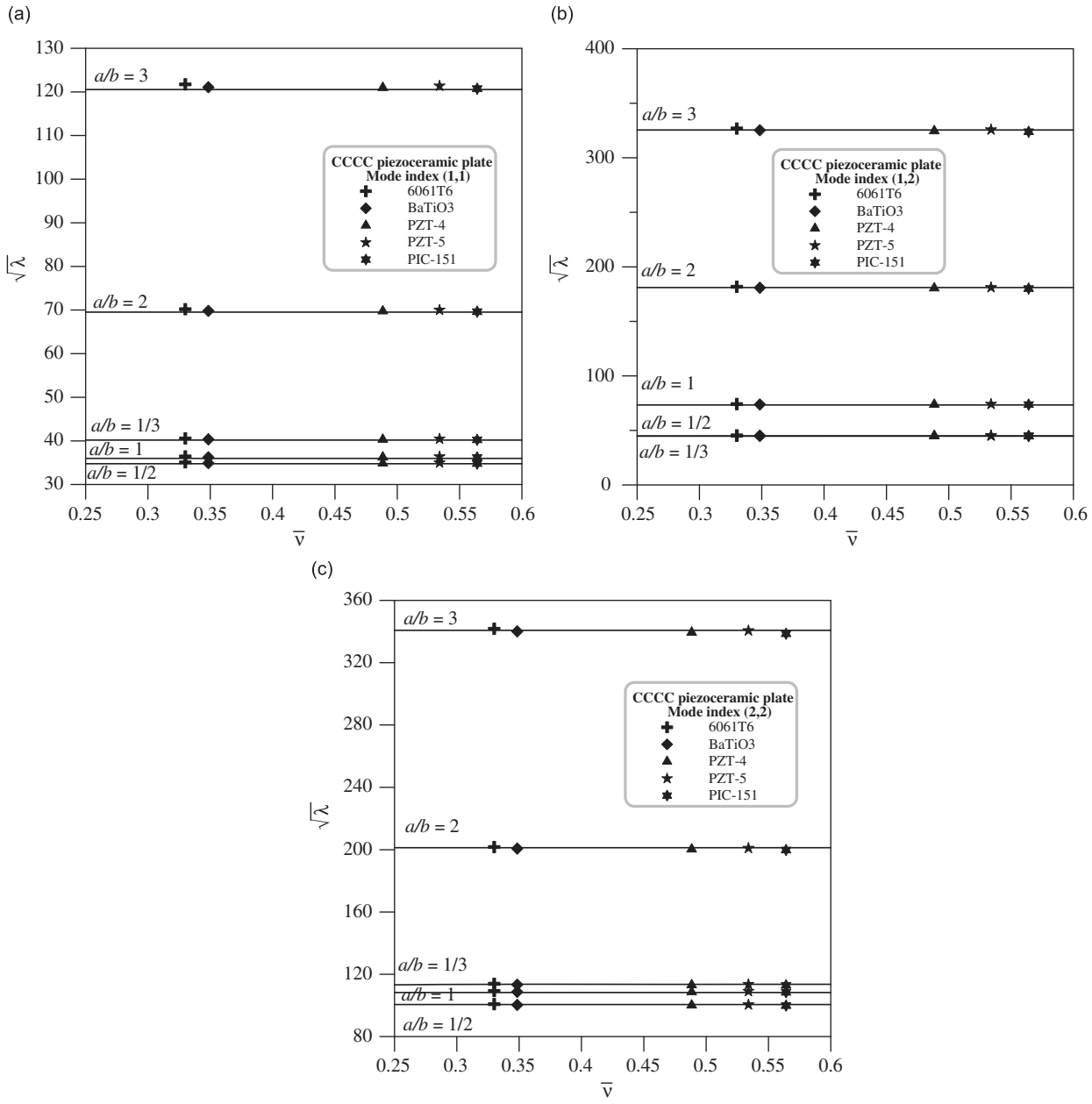

Fig. 7. Frequency parameter ($\sqrt{\lambda}$) versus equivalent Poisson's ratio ($\bar{\nu}$) for the mode indices: (a) (1,1), (b) (1,2), and (c) (2,2) with different aspect ratios (a/b).

frequency parameter ($\sqrt{\lambda}$) is plotted as the ordinate to exhibit the frequency variation for constant aspect ratio; and five different aspect ratios ($a/b = \frac{1}{3}, \frac{1}{2}, 1, 2$, and 3) are employed for the theoretical calculations. To verify the validity of the proposed theoretical methodology, one isotropic aluminum material (6061T6) and four piezoceramic materials ($BaTiO_3$, PZT-4, PZT-5, and PIC-151) are selected to perform the calculations by FEM. Their material properties are listed in Table 1. As shown in Fig. 6, the frequency parameter λ decreases when the equivalent Poisson's ratio $\bar{\nu}$ increases, except for mode (3,1) with $a/b = 1$. Figs. 7(a)–(c) show the frequency parameter variations of the CCCC piezoceramic plate for mode indices (1,1), (1,2), and (2,2). It is noted that, by theoretical calculation, the frequency parameter does not depend upon the Poisson's ratio $\bar{\nu}$ with the completely clamped boundary. However, the resonant frequency depends upon $\bar{\nu}$ because the flexural rigidity $\bar{D}$ contains $\bar{\nu}$. In light of this result, the errors for the CCCC piezoceramic plate between theoretical and numerical calculations are smaller than those for the FFFF piezoceramic plate shown in Fig. 6. In Fig. 7(b), it is noteworthy that the curves for $a/b = \frac{1}{3}$ and $\frac{1}{2}$ are very close to each other and this also occurs for the FEM calculations. However, the nearly

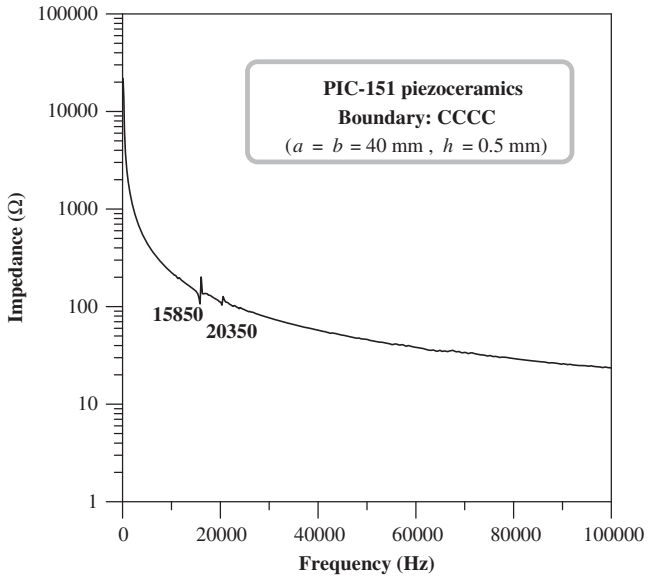

Fig. 8. Impedance variation curves of the FFFF piezoceramic plate.

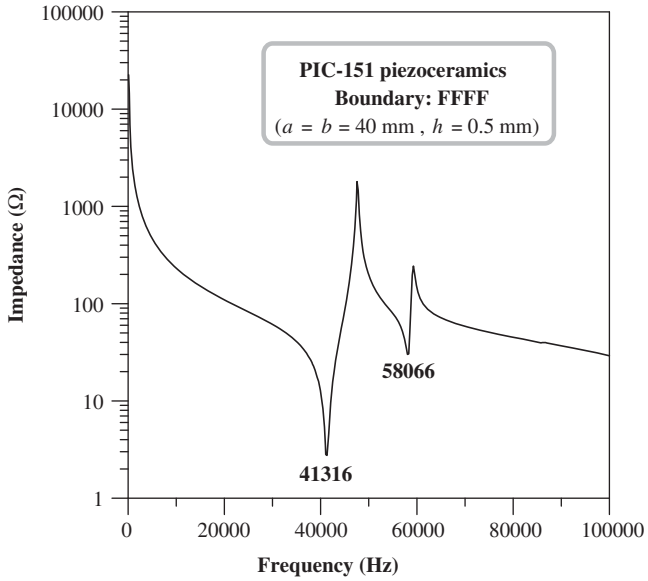

Fig. 9. Impedance variation curves of the CCCC piezoceramic plate.

identical value $\sqrt{\lambda}$ for two different aspect ratios a/b will result in two distinct resonant frequencies that depend on the dimensional term $\sqrt{a^3 b}$.

Figs. 8 and 9 show the impedance variations of the FFFF and CCCC piezoceramic plates, respectively, where experimental results are obtained by an impedance/gain-phase analyzer HP-4194A (Hewlett Packard). The local minima and maxima appearing in the impedance curve correspond to the resonant and anti-resonant frequencies, respectively. It is significant that the resonant frequencies shown in Fig. 8 are much higher than those shown in Table 2 for transverse vibration modes. With the aid of FEM analysis, these two vibration modes shown in Fig. 8, as measured by impedance analyzer, are the in-plane extensional modes. This reveals that the transverse vibration modes of the FFFF piezoceramic plate cannot be obtained by impedance analysis. On the other hand, the two vibration modes that indicated in Fig. 9 are not extensional modes but transverse modes, because the resonant frequencies correspond to the modes (2,5) and (1,6) in Table 3. As compared with the case of the FFFF piezoceramic plate, it can be seen that the transverse modes for the CCCC piezoceramic plate, as measured by impedance analysis, are induced due to the clamped edges. In other words, inasmuch as the

imperfect clamped boundary simulation, the transverse modes will be unexpectedly detected with the impedance variation.

5. Conclusions

Concerning the rectangular plates with completely free and completely clamped boundaries, it is analytically difficult to obtain exact solutions for the vibration analysis, even for an isotropic material. Herein Ritz's method together with equivalent constants provides a more convenient strategy to investigate the transverse vibration characteristics of piezoceramic rectangular plates. The advantages of using this methodology are that the electrical field consideration can be neglected, and the vibration analysis of piezoceramic plates is carried out once the corresponding conditions of isotropic plates are given. By means of the numerical calculations and two experimental measurements (AF-ESPI and LDV) employed in this study, consistency between these results implies that the theoretical prediction has good accuracy and gives the upper bounds for most of the transverse resonant frequencies. With the different aspect ratios and material types of piezoceramic plates, the frequency parameter variations are theoretically discussed and agree well with the FEM calculations. In addition, it is experimentally found that the impedance analyzer cannot measure the transverse vibration modes of piezoceramic plates; however, if the clamped boundary simulation is imperfect, the transverse vibration modes will be unexpectedly measured.

Acknowledgment

The authors gratefully acknowledge the financial support of this research by the National Science Council (Republic of China) under Grant NSC 94-2212-E-231-004.

References

[1] M.C. Dökmecí, Vibration of piezoelectric crystals, *International Journal of Engineering Science* 18 (1980) 431–448.
[2] N.N. Rogacheva, *The Theory of Piezoelectric Shells and Plates*, CRC Press, Boca Raton, FL, 1994.
[3] N.F. Ivina, Numerical analysis of the normal modes of circular piezoelectric plates of finite dimensions, *Soviet Physics Acoustics* 35 (1990) 385–388.
[4] C.H. Huang, C.C. Ma, Y.C. Lin, Theoretical analysis and experimental measurement for resonant vibration of piezoceramic circular plates, *IEEE Transactions on Ultrasonics, Ferroelectrics and Frequency Control* 51 (2004) 12–24.
[5] C.H. Huang, Transverse vibration analysis and measurement for the piezoceramic annular plate with different boundary conditions, *Journal of Sound and Vibration* 283 (2005) 665–683.
[6] R. Holland, Contour extensional resonant properties of rectangular piezoelectric plates, *IEEE Transactions on Sonics and Ultrasonics* SU-15 (1968) 97–105.
[7] J.S. Lee, L.Z. Jiang, Exact electroelastic analysis of piezoelectric laminae via state space approach, *International Journal of Solids and Structures* 33 (1996) 977–990.
[8] W.Q. Chen, R.Q. Xu, H.J. Ding, On free vibration of a piezoelectric composite rectangular plate, *Journal of Sound and Vibration* 218 (1998) 741–748.
[9] R.C. Batra, X.Q. Liang, The vibration of a rectangular laminated elastic plate with embedded piezoelectric sensors and actuators, *Computers and Structures* 63 (1997) 203–216.
[10] S.H. Chang, Y.C. Tung, Electro-elastic characteristics of asymmetric rectangular piezoelectric laminae, *IEEE Transactions on Ultrasonics, Ferroelectrics and Frequency Control* 46 (1999) 950–960.
[11] C.C. Ma, H.Y. Lin, Experimental measurements on transverse vibration characteristics of piezoceramic rectangular plates by optical methods, *Journal of Sound and Vibration* 286 (2005) 587–600.
[12] F. Ramirez, P.R. Heyliger, E. Pan, Free vibration response of two-dimensional magneto-electro-elastic laminated plates, *Journal of Sound and Vibration* 292 (2006) 626–644.
[13] F. Ramirez, P.R. Heyliger, E. Pan, Discrete layer solution to free vibrations of functionally graded magneto-electro-elastic plates, *Mechanics of Advanced Materials and Structures* 13 (2006) 249–266.
[14] C.H. Huang, Resonant vibration investigations for piezoceramic disks and annuli by using the equivalent constant method, *IEEE Transactions on Ultrasonics, Ferroelectrics and Frequency Control* 52 (2005) 1217–1228.
[15] D. Young, Vibration of rectangular plates by the Ritz method, *Journal of Applied Mechanics* 17 (1950) 448–453.
[16] W.C. Wang, C.H. Hwang, S.Y. Lin, Vibration measurement by the time-averaged electronic speckle pattern interferometry methods, *Applied Optics* 35 (1996) 4502–4509.
[17] C.H. Huang, C.C. Ma, The investigation of three-dimensional vibration for piezoelectric rectangular parallelepipeds by using the AF-ESPI method, *IEEE Transactions on Ultrasonics, Ferroelectrics and Frequency Control* 48 (2001) 142–153.
[18] *ABAQUS User's Manual*, *Version 6.3*, Hibbitt, Karlsson and Sorensen, Inc., Rhode Island, 2002.